Agora of Additive Manufacturing (2024) paper24001

JAMS

Agora of Additive Manufacturing

journal homepage: http://additive-manufacturing.or.jp/

New 3D printer for molding continuous-fiber composites using coaxial double nozzles

Akira Todoroki [a*], Kota Hayakawa [a], Masato Ueda [b], Ryosuke Matsuzaki [c], Keisuke Iizuka [d]

[a] Department of Mechanical Engineering, Tokyo Institute of Technology, Tokyo, Japan

[b] Department of Mechanical Engineering, College of Science and Technology, Nihon University, Tokyo, Japan

[c] Department of Mechanical and Aerospace Engineering, Faculty of Science and Technology, Tokyo University of Science, Chiba, Japan

[d] Department of Mechanical Engineering, Faculty of Science and Engineering, Aoyama Gakuin University, Kanagawa, Japan

ABSTRACT

Commercially available three-dimensional (3D) printers for continuous-fiber composites feature twin nozzles (one for short fibers (or resin) and the other for continuous fibers). When designers use nonuniformly curved patterns for continuous fibers, inevitable gaps between printing paths cause initial defects. To address this challenge, we developed 3D printer hardware with coaxially arranged nozzles for continuous and short-fiber filaments. This arrangement allows the adjustment of the amount of the short-fiber (or resin) along the continuous-fiber path, preventing print path gaps. The short-fiber nozzle uses a screw and pellets instead of filaments, with a hole at the center of the screw for printing continuous fibers. After modifying the printing conditions, we fabricated unidirectional specimens using the proposed 3D printer and conducted tensile tests, which confirmed its effectiveness for printing continuous-fiber composites.

Keywords: Carbon fiber, 3D printing, additive manufacturing, twin-nozzle system, thermoplastics

1. Introduction

The Mark One® is a three-dimensional (3D) printer that fabricates continuous-fiber thermoplastics using the fused filament fabrication (FFF) method. It was first unveiled in January 2014 at the SolidWorks World Design Conference in the United States [(1)]. In June 2014, Namiki et al. [(2)] attempted composite molding using an in-house 3D printer that molds continuous-fiber-reinforced thermoplastic composite materials. Furthermore, Matsuzaki et al. [(3)] and Tian et al. [(4)] developed 3D printers that use a continuous-fiber nozzle-impregnated composite material using a modified 3D printer. They demonstrated that composite materials comprising continuous fibers can be 3D printed using the FFF method.

Van Der Klift et al. [(5)] evaluated the tensile strength of continuous-fiber composites fabricated using Mark One®, which is the first product of Markforged. The Mark One® exhibited significant variations in strength owing to problems with the initial slicing software that determines the fiber arrangement of the 3D printer. In 2017, Markforged released Mark Two®, which facilitated the 3D printing of continuous-fiber-reinforced composites with relatively free fiber arrangements [(6)]. Mark Two® allows users to select from two types of continuous-fiber arrangement methods: unidirectional and spiral or a mixture of both. Todoroki et al. [(7)] reported the tensile strength of continuous-fiber composites molded using Mark Two®.

As an example of the application of 3D-printed continuous-fiber composites, Yamanaka et al. [(8)] demonstrated the possibility of reducing the stress concentration around an open hole and improving the strength by bending the fibers in

* Corresponding author
Email: todoroki.a.aa@m.titech.ac.jp
Received 27 March 2024; Revised 23 May 2024; Accepted 11 June 2024
Available online 26 July 2024

various ways during fabrication. However, in commercially available Markforged 3D printers, the nozzles for short fibers (or resin) and continuous fibers are positioned differently, creating large gaps between adjacent paths with different curvatures. Therefore, it is impossible to realize a fiber bundle arrangement in which the curvatures of adjacent fiber bundles are different, as observed in the results obtained by Yamanaka et al. [8].

Thus, in this study, we developed a 3D printer for fabricating composite materials in which the outer nozzle for molding short fibers and the inner nozzle for molding continuous fibers are arranged coaxially. This allows the injection amount of short fibers to vary depending on the location. To verify the operation of the proposed 3D printer for molding composite materials, rectangular specimens were prepared for tensile tests, and the effectiveness of continuous-fiber reinforcement was confirmed.

2. Basic design of proposed 3D printer

2.1 Basic concepts

Fig. 1 shows a schematic representation of the printhead of the proposed 3D printer. The printer ejects short-fiber-reinforced resin and long fibers coaxially to perform 3D printing. The short fibers are typically provided as pellets because of the low cost of pellets. Thus, a screw mechanism is used to supply the pellets. A small hole is drilled through the center of the screw shaft, and a pipe is passed through the hole. Thereafter, the pipe is positioned coaxially with the screw as a nozzle for the continuous fibers.

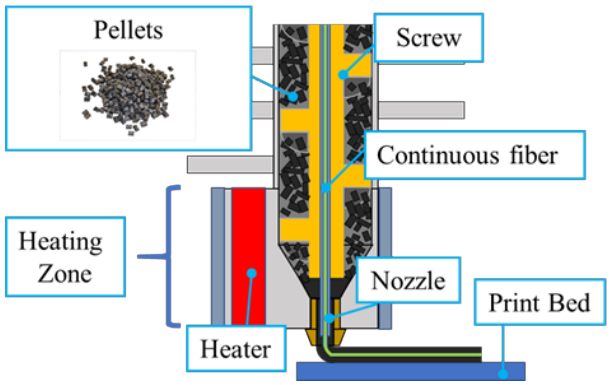

Fig. 1 Schematic representation of the proposed 3D printer.

To vary the mass of the short-fiber composites, the screw rotation speed was changed. This enabled us to cover continuous fibers with short fibers by changing the injected mass depending on the fabrication location. Even when the print path distance changed, the injected short-fiber was changed to fill the gaps.

Here, a continuous carbon fiber-reinforced polymer (CFRP) filament (Markforged, fiber volume fraction of approximately *30* %) was used. Considering that this filament uses PA-6 resin, carbon fiber PA-6ellets (3DX Tech) were used as short-fiber-reinforced resin pellets. The fiber volume fraction of this material was approximately *15* %.

2.2 Screw design

Fig. 2 shows a 3D model of the designed screw, and Table 1 presents the properties of the screw. The screw shape was intended to efficiently supply resin pellets to the heating and melting sections; thus, a single screw without a compression ratio was adopted [9][10]. In addition, considering that the size of the resin pellets was approximately *3.5* mm, the screw groove depth was *4.5* mm, and the screw pitch was 26. A small hole (diameter = *1.4* mm; length = *175.3* mm) was made through the center of the screw shaft to allow the long fibers and metal pipe to pass through.

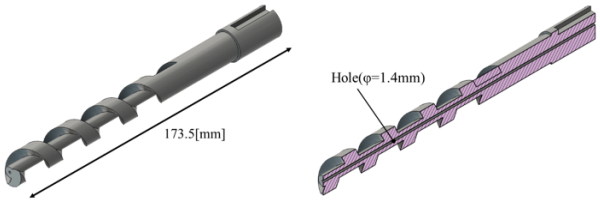

Fig. 2 Screw design.

Table 1. Screw Properties

Screw properties	Values
Screw length [mm]	114
Screw diameter [mm]	15
Screw pitch [mm]	26
Hole diameter [mm]	1.4
Channel depth [mm]	4.5
Compression ratio	1
Channel	Single

2.3 Heat block design

To design the heat block, the thermal properties of the short-fiber-reinforced resin pellets were determined. A differential scanning calorimeter (DSC-60plus, Shimadzu Corp.) was used. The experiments were performed in accordance with JIS K7121-7123, and the melting point, heat of fusion, and specific heat of the material were determined (Table 2).

Table 2 Thermal properties of carbon fiber Nylon 6 pellets

Thermal properties [unit]	Measured results
Melting point [°C]	221.6
Melting heat [J/g]	29.5
Specific heat [J/kg K]	$6.48T + 968$

Let us assume that the 3D printing is in a thermally steady-state. In the steady-state, an injection device, such as the screw, exhibits a steady temperature. Thus, the amount of heat input required by the heater is the sum of the heat (Q_1) required to increase the temperature of the pellets to their melting point and the heat of fusion (Q_2) required to melt the pellets. In addition, because the pellets melt as the screw feeds them, the heater capacity that provides the required heat per unit time is equal to the amount of heat required to melt the resin transported by the screw per unit time. The density (ρ) and specific heat (C_p) can be calculated using the following equations. This is based on the temperature at the end of the heating period (T_f), temperature at the beginning of the heating period (T_s), heat of fusion of the pellets (Q), and volume of the pellets flowing into the screw per second (q).

$$Q_1 = \int_{T_s}^{T_f} q\rho C_p dT. \tag{1}$$

$$Q_2 = q\rho Q. \tag{2}$$

q was set to *20* mm^3/s based on the filament extrusion speed of the filament manufacturing machine (FILASTRUDER). The C_p, Q, and end-of-heating temperature were obtained from Table 2. The initial heating temperature was set to *20* °C. The calculations yielded $Q_1 = 78.7$ J/S and $Q_2 = 6.90$ J/S. Some heat was lost via heat transfer through the carbon fibers of

the pellets; thus, the safety factor of the thermal design was set to *3*, and the required heat capacity of the heater was set to *250* W.

Fig. 3 shows the designed heating area. The heating area heats and melts the resin; thus, all the parts were made of metal. The barrel and heat block, which heat and melt the resin, were made of aluminum alloy A5052, which exhibits high thermal conductivity. The mount part, which is fixed to the plastic hopper, was made of SUS304, which exhibits low thermal conductivity, to prevent heat transfer. Brass, frequently used in general-purpose FFF-type 3D printers, was used for the nozzle. A heat sink (diameter = *30* mm; thickness = *1.5* mm) was attached to the barrel to reduce the heat transfer to the top of the barrel. This was because the hopper attached to the mount part was made using a resin-based 3D printer and fabricated using short carbon fiber, PA-6. In the designed heating parts shown in Fig. 3, steady-state heat transfer was expected during the steady-state printing process. Thus, a steady-state analysis of the heating area was conducted using Ansys Workbench 18.1. The analysis was based on the assumption that the heater temperature was *240* °C (*20* °C above the melting point of the material) and that the sides of the heat block were covered with insulating material (heat transfer coefficient set to *0*). The heat transfer coefficient of the heat sink was set to *30* W/(m^{2}K), assuming forced air convection.

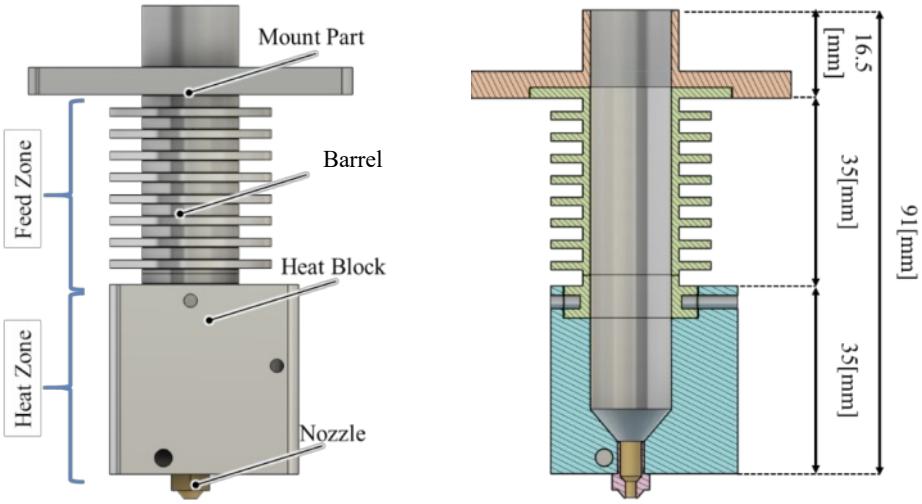

Fig. 3 Schematic representation of heating area.

Fig. 4 shows the results of the steady-state analysis. In the designed heating region, the temperature of the feed zone gradually increased from top to bottom. Furthermore, because the heat zone reached a temperature range of *227–240* °C (exceeding the melting point of PA-6 (*220* °C)), we determined that the PA-6 heated through the feed zone can be melted in the heat zone. The temperature of the mount part was *87* °C, and the continuous use temperature of the structural material (PA-6) of the hopper was in the range of *80–150* °C. The load on this part was only the weight of the hopper and the weight of the pellets; thus, we conclude that continuous use is entirely possible even in the designed heating region.

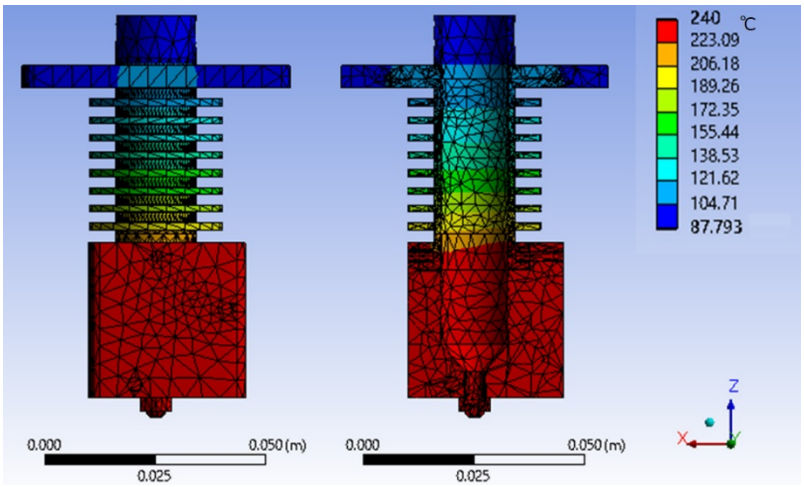

Fig. 4 Finite element method analysis results of heated parts.

2.4 Motor and gear settings

The proposed 3D printer uses a coaxial double nozzle mechanism. Thus, a pipe for the continuous-fiber passes through the coaxial hole of the screw, and the space above the screw is used as the feed space for the fiber. Therefore, the motor that rotates the screw is positioned away from the screw shaft, and the resin is heated and melted as the screw rotates, thereby increasing its viscosity. It has been reported that viscosity increases when reinforcing fibers are combined with the base resin; thus, a high torque is required to rotate the screw [(11)].

Therefore, a worm gear was used. Considering that the worm gear comprised two parts, a worm and worm wheel, there was no need to place the motor on the screw axis. Furthermore, compared with other gears, the worm gear is more likely to achieve a large reduction ratio and can generate high torque, rendering it suitable for the proposed 3D printer. Equation (3) was used to calculate the output after deceleration.

$$T_2 = T_1 i \eta_R. \tag{3}$$

T_1 is the motor torque, T_2 is the output torque, i is the reduction ratio, and η_R is the transmission efficiency of the worm gear when driven from the worm side [(12)]. Generally, the transmission efficiency is within the range of *0.3–0.9* and is *0.5* or less in the low-speed range [(13)]. Here, it was set to *0.4* as a design guideline.

The T_1 required to calculate T_2 was calculated with two types of output torque (*0.4* and *1.19* Nm), using the Nema 17 stepping motor (frequently used in general-purpose 3D printers) and the Nema 23 stepping motor (higher output torque). The reduction ratio was calculated by varying the reduction ratio of commercially available worm gears in the range of 10–*60*. The target output torque was set to a motor torque of *15.6* Nm, which is the setting used in the commercially available filament molding machine, FILASTRUDER [(14)]. As a high-output torque was required, the Nema23 motor was determined appropriate for obtaining a motor torque of *15.6* Nm. The target value could be achieved by setting the reduction ratio to *40* or above. Here, a worm gear with a reduction ratio of *40* was used.

2.5 Printhead

Fig. 5 shows an image of the designed printhead. Fig. 6 shows the external dimensions and cross-section of the printhead.

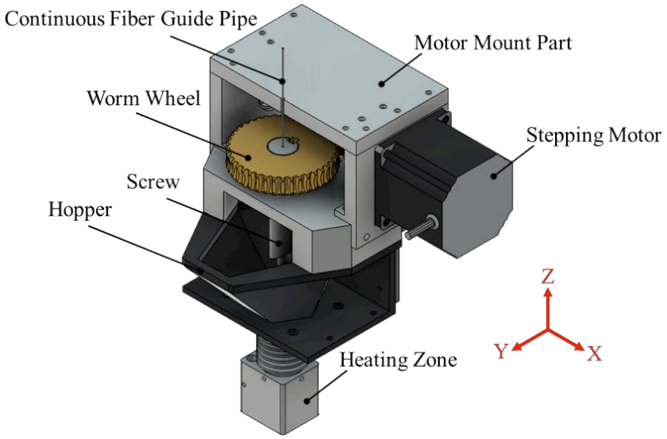

Fig. 5 Designed printhead.

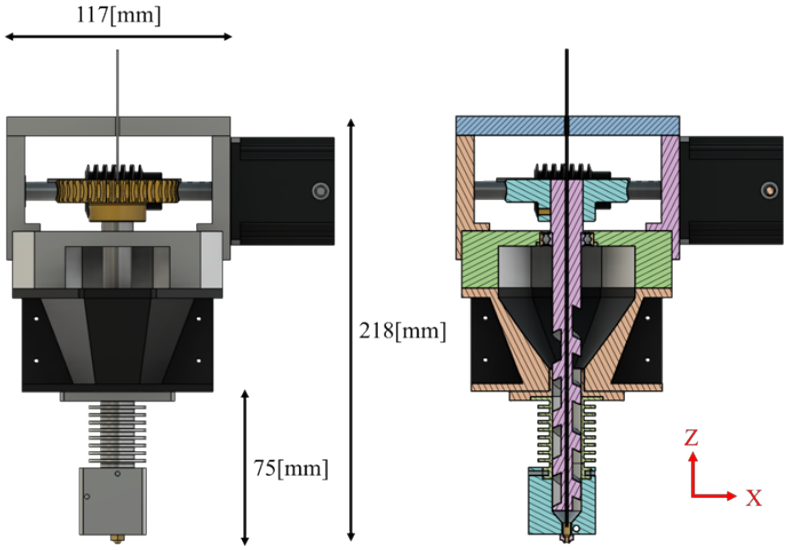

Fig. 6 Dimensions and cross-sectional view of printhead.

Considering the ease of installation and control of the printhead of the proposed 3D printer, we selected the Velleman K8200 3D printer as the body. Fig. 7 shows the complete 3D printer.

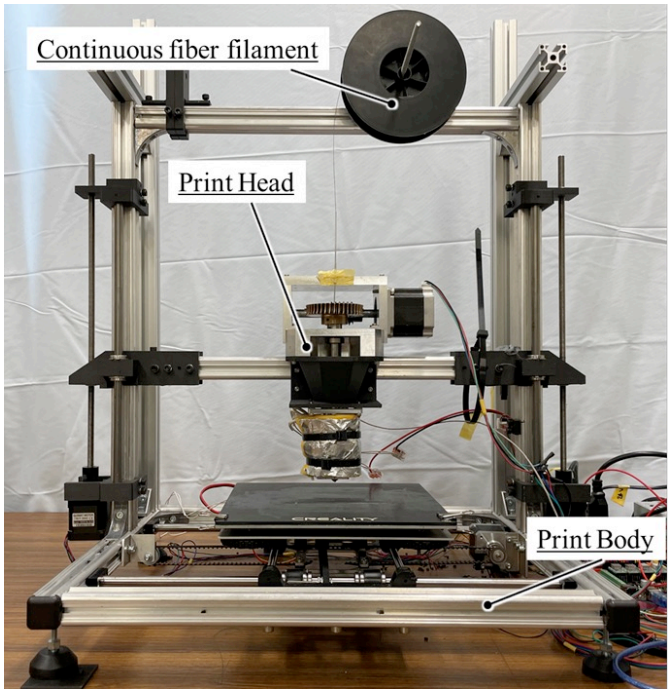

Fig. 7 Appearance of proposed 3D printer.

The 3D printer requires control of the *X*, *Y*, and *Z* axes, rotation control of the screw in the extruder section, and temperature control of the heating area. The difference between this printer and a general-purpose FFF 3D printer is the high motor current in the extruder section and the heater capacity. Thus, we adopted the Megatronics v3.3 control board (RepRap) (hereinafter referred to as Megatronics), which features an easy-to-replace motor driver. Considering that Megatronics can use an external driver for motor control that requires a higher current than usual, it was possible to use the TB6600 (SainSmart) motor driver, which can control the Nema 23 used in the extruder section. In addition, because the output of Megatronics was insufficient, we adopted the MTCD (MISUMI) temperature controller to control the temperature of the heater. This controller can use a *100* V-driven heater; this allowed us to use the high-output heater required for the 3D printer.

Using the proposed 3D printer, we printed continuous carbon fiber/PA-6 and short carbon fiber/PA-6 to optimize the printhead temperature, molding speed, and tip position of the inner pipe of the coaxial double nozzle. A nozzle with a diameter of *2.4* mm was used, considering that the pipe would pass through the inside. After trial-and-error experiments, a printhead temperature of *240* °C and molding speed of *100* mm/min were determined as conditions that minimized the occurrence of voids between paths and deviations in the continuous fibers. The screw rotation speed was *3.5* min^{-1}.

The position of the pipe for the continuous-fiber in the screw could be set independently of the screw tip. This pipe was used to protect the continuous-fiber and adjust the position at which it was injected. If the continuous-fiber were supplied without a pipe, it would rub against the edge of the rotating screw. The primary purpose of using the pipe was to prevent this damage. The secondary purpose was to adjust the position of the pipe tip such that the continuous-fiber was embedded in the center of the path of the thermoplastic resin injected by the screw. Without the pipe, the continuous-fiber would bend in the direction of the path from the screw hole and be positioned above the path of the injected thermoplastic resin. The pipe was installed to adjust the position of the continuous-fiber (see Appendix).

Three types of pipe position adjustments were experimentally examined: Types A, B, and C, in which the pipe tip was placed *1* mm in the nozzle tip, *0.2* mm beyond the nozzle tip, and *0.5* mm beyond the nozzle tip, respectively. However, because the material was not uniformly extruded if the screw extrusion amount was small, the distance between the nozzle and bed (layer pitch) was set to *0.6* mm. The Type B state was set to less than half the layer pitch, whereas the Type C state

was set to between half the layer pitch and the layer pitch. The Type B position, which experimentally produced the fewest voids, was selected (see Appendix). Table 3 lists the selected molding conditions. It should be noted that a fiber-cutting device was not installed on the proposed 3D printer.

Table 3 Three-dimensional printing conditions used in this study

3D printing conditions [unit]	*Value*
Nozzle temperature [°C]	*240*
Print speed [mm/min]	*100*
Distance between print paths [mm]	*2.4*

3. Verification of effectiveness through strength testing

Using the proposed 3D printer, test specimens containing a mixture of continuous and short fibers were prepared. In addition, 0° tensile tests, in which a tensile load was applied in the direction of the continuous fibers, and 90° tensile tests, in which a tensile load was applied perpendicular to the fiber direction, were performed.

3.1 Preparation of test specimens

The proposed 3D printer was not equipped with a function for cutting continuous fibers. Thus, when preparing the plate-shaped test specimen, the fibers were continuously molded to avoid cutting, and the curved portions of the fiber bundles were removed after molding. For example, Fig. 8 shows a schematic diagram of the print path of a 0° layer tensile test specimen. A unidirectional continuous-fiber path was created by bending the continuous fibers at their ends on the print bed. When moving to the upper layer, the nozzle was raised at the end of the specimen and a unidirectional continuous-fiber path was started without cutting the fibers. Through this method, the continuous fibers were connected in the stacking direction at the ends. Thus, the ends were cut to conduct tensile tests.

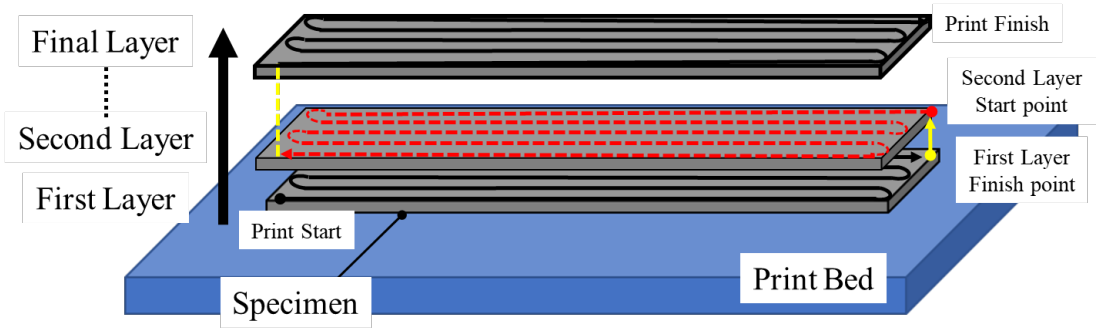

Fig. 8 Example of a print path for the fabrication of unidirectional composite specimens.

The test specimen was *120* mm long × *16.8* mm wide × *2.4* mm thick, with a print path distance of *2.4* mm and a layer pitch of *0.6* mm, with four layers laminated. Under these fabrication conditions, the volume fraction of continuous fibers, when using continuous-fiber filaments, was approximately *3* %. After 3D printing, both ends of the test specimen were cut by *5* mm to eliminate the influence of the ends, and the test specimens were only fabricated in the *0*° direction. Three test specimens were fabricated using only short-fiber-reinforced resin, and three were formed using long fibers. The tests were conducted by bonding *1.5*-mm-thick glass fiber-reinforced polymer (GFRP) tabs to the *25*-mm sections at both ends of the test specimens. Uniaxial strain gauges were attached to both sides of the center of the test specimen to measure the strain in the tensile direction.

Fig. 9 shows the *90*° test specimen, which was *120* mm long × *15* mm wide × *1.8* mm thick, with a print path distance of *2.4* mm and a layer pitch of *0.6* mm. The specimen was fabricated through three layers of lamination. To eliminate the

influence of the folded fiber bundle, the ends were cut at 5-mm intervals after 3D printing to prepare the test specimens. Similar to the 0° test specimens, three test specimens were fabricated using only short-fiber-reinforced resin, and three were prepared using long fibers. GFRP tabs (thickness = *1.5* mm) were attached to both ends of the fabricated test specimens, *25* mm from each end, and the test was performed. Uniaxial strain gauges were attached to both sides of the center of the test specimen to measure the strain in the tensile direction.

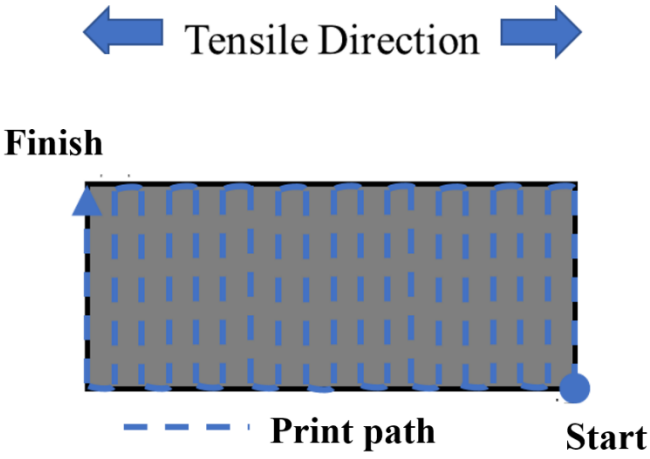

Fig. 9 Print path of 90° specimen.

The test specimens prepared using the aforementioned procedures were subjected to tensile tests using a universal tester (AUTOGRAPH AG-I 100kN, Shimadzu Corp.) at a test speed of 1 mm/min. To avoid the effects of moisture absorption, the specimens were stored in a desiccator at a humidity level of *10* % or less for more than *72* h after preparation prior to the tests.

3.2 Tensile tests

Fig. 10 shows the stress–strain curves obtained from the tensile tests. Figs. 10 (a) and 10 (b) show the stress–strain relationship of the specimens with and without (only short fibers) continuous fibers in the 0° direction, respectively. Figs. 10 (c) and 10 (d) show the results of the specimens with and without (only short fibers) continuous fibers in the *90*° direction, respectively.

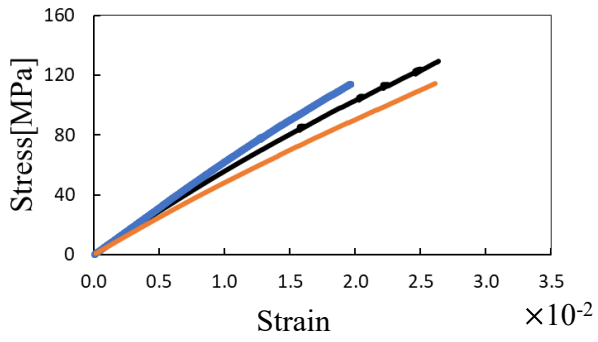

(a) *0*° specimen with continuous carbon fibers.

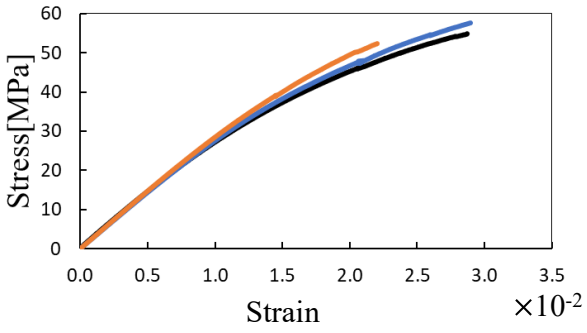

(b) *0*° specimen without continuous carbon fibers (short-fiber composites)

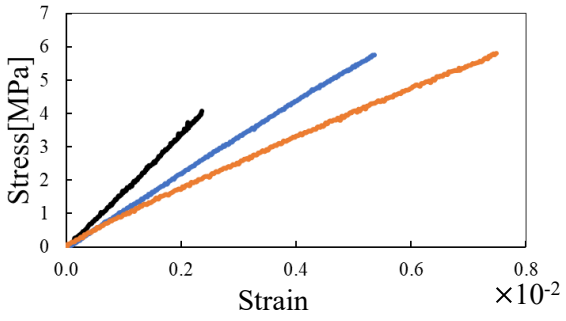

(c) *90°* specimen with continuous carbon fibers.

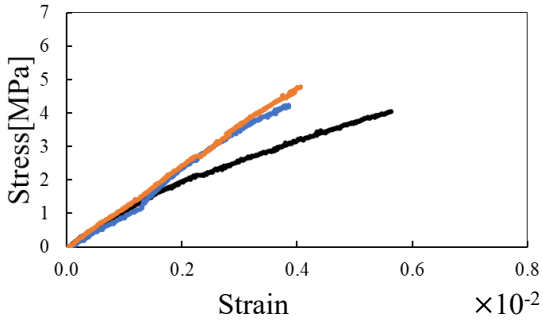

(d) *90°* specimen without continuous carbon fibers (short-fiber composites).

Fig. 10 Stress–strain curves of tensile test specimens.

Table 4 Mechanical properties of *0°* orientation specimen

	0° orientation specimen with continuous fibers	*0° orientation specimen without continuous fibers*
Tensile strength [MPa]	*121.4*	*54.9*
(Standard deviation)	*(6.14)*	*(2.18)*
Elastic modulus [GPa]	*5.74*	*2.95*
(Standard deviation)	*(0.49)*	*(0.04)*

Table 5 Mechanical properties of *90°* direction specimen

	90° orientation specimen with continuous fibers	*90° orientation specimen without continuous fibers*
Tensile strength [MPa]	*5.22*	*4.35*
(Standard deviation)	*(0.81)*	*(0.31)*
Elastic modulus [GPa]	*1.31*	*1.12*
(Standard deviation)	*(0.27)*	*(0.06)*

Tables 4 and 5 present the average values and standard deviations of the mechanical properties of the *0°* and *90°* specimens, respectively. Fig. 11 shows the appearance of each specimen after fracturing.

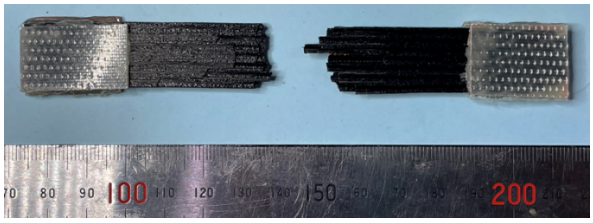

(a) *0*° specimen with continuous carbon fibers.

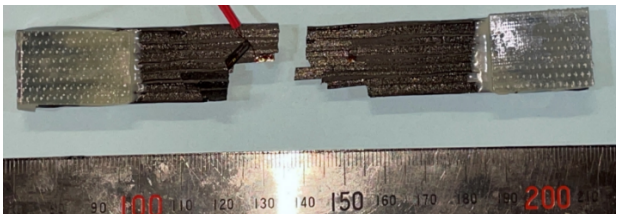

(b) *0*° specimen without continuous carbon fibers (short-fiber composites).

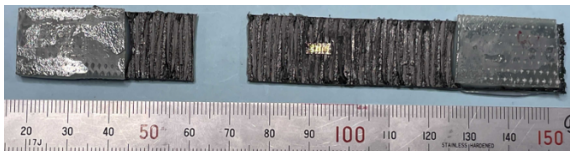

(b) (c) *90*° specimen with continuous carbon fibers.

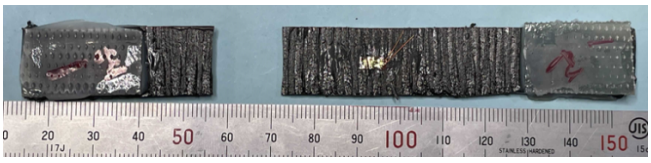

(d) *90*° specimen without continuous carbon fibers (short-fiber composites).

Fig. 11 Specimens after tensile tests.

For the *0*° direction (fiber orientation) of the composite containing continuous fibers, the slope of the stress–strain relationship differed for each specimen, resulting in a variation in the elastic modulus. However, the stress–strain relationship was only slightly nonlinear in the high-stress region. The elastic modulus and strength in the *0*° direction are subsequently discussed.

In the extrusion direction of the short carbon fiber PA-6 without continuous fibers (Fig. 10 (b)), a nonlinear stress–strain relationship was observed. The elastic modulus and tensile strength were *2.95* GPa and *54.9* MPa, respectively (Table 4). In the *90*° direction (Table 5), the elastic modulus was *1.12*. The compressive strength of the fiber was *4.35* GPa, which was practically one-third of the original strength. The tensile strength was *4.35* MPa, which was less than one-tenth of the original strength. As reported by Koga et al. [(15)], this was caused by the anisotropy that occurs when short fibers are aligned in the ejection direction from the nozzle (print path direction) during 3D printing.

The elastic modulus with continuous fibers in the 0° direction was *5.74*, and the tensile strength was *122* MPa. The continuous-fiber was used as a continuous-fiber filament with a fiber volume fraction of approximately *30* %. The continuous-fiber-reinforced PA-6 filament occupied *10* % of the volume of one print path. The measured tensile strength of the Markforged continuous-fiber-reinforced PA-6 filament in the 0º direction was *701* MPa, and the elastic modulus was *60*. Considering that the elastic modulus was *1* GPa, it was calculated using the rule of mixtures [(8)], with the following equation, assuming that the volume fraction of the continuous-fiber filaments is $V_{CF} = 10$ %:

$$E_L = E_{C0}V_{CF} + (1 - V_{CF})E_{S0} = 60 \times 0.1 + 0.9 \times 2.95 = 8.7 \text{ GPa}. \quad (4)$$

The strength was calculated using the following equation:

$$\sigma_L = \sigma_{C0} V_{CF} + (1 - V_{CF})\sigma_{S0} = 701 \times 0.1 + 0.9 \times 54.9 = 120 \text{ MPa}. \quad (5)$$

Comparing the results calculated using the mixture rule with the measured values, the tensile strength was practically consistent with the measured value (*121* MPa). This showed that the continuous fibers were effective and that fiber breakage during molding did not occur to a problematic degree. The measured elastic modulus (*5.74* GPa) was slightly smaller than the calculated value (*8.7* GPa). Owing to the variation in the stress–strain relationship, it was determined that the strain gauge did not correctly measure the average tensile strain because of the influence of the warping of the test piece, surface unevenness, and the volume fraction of the continuous fibers being only *3*%. In addition, the mixture rule of Equation (4) does not consider the effects of voids; however, a mixture rule [16] that considers voids exists. Here, we were unable to observe the detailed distribution of voids in the test piece; therefore, we will include a detailed observation of the void distribution in the future.

Furthermore, as shown in Figs. 11(a) and (b), vertical cracks occurred on the fracture surface in the print path direction. This implied that the fusion between the print paths was insufficient; thus, further optimization of the molding conditions is necessary.

The *0*° test piece containing continuous fibers was subjected to X-ray computed tomography (CT, Comscan Techno, ScanXmate-L080HT, *1* pixel per *50* μm) (Fig. 12). The vertical direction in the image is the fiber direction of *0*°, and black shadows of voids can be observed along the fiber orientation. Fig. 13 shows the results of the X-ray CT observations of only the short carbon fiber composite. Voids were observed between the print paths, indicating that the fusion between the print paths was insufficient.

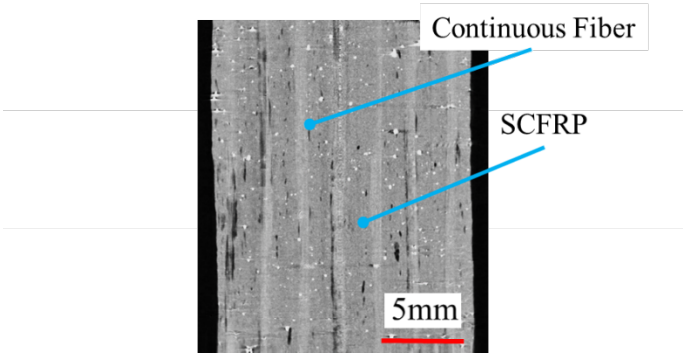

Fig. 12 X-ray CT observation result of *0*° specimen with continuous carbon fibers.

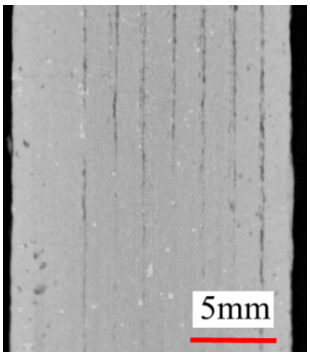

Fig. 13 X-ray CT observation result of *0*° specimen without continuous carbon fibers.

To measure the void ratio, a cross-sectional observation was performed on the *0*º test specimen containing continuous fibers. The test specimen in this study was a composite of continuous and short carbon fibers; thus, the combustion method

was not employed, and the void ratio was measured from the cross-sectional image. Fig. 14 shows a cross-sectional image of the *0*° test specimen containing continuous fibers. Black areas were observed between the print paths and voids.

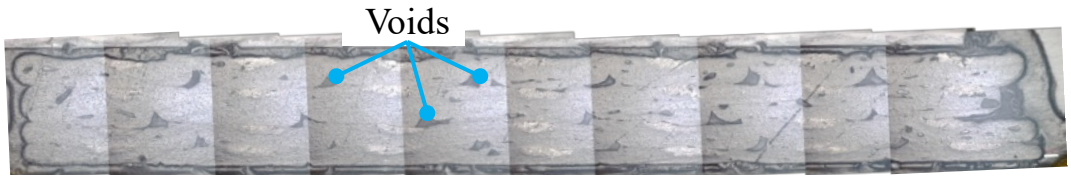

Fig. 14 Cross-sectional observation of *0*° specimen with continuous carbon fibers.

A void fraction of *6.8*% was measured using the ImageJ image processing software on the observation results. Van Der Klift et al. stated that the void fraction was approximately *7*% based on cross-sectional observations of a Mark One continuous-fiber test piece [(5)]. Thus, the void fraction did not improve, and it was considered that this affected the error between the measured and calculated elastic moduli. However, the void fraction could be improved by adjusting the molding conditions, which is a future challenge.

4. Conclusions

The purpose of this study was to develop a 3D printer for molding composite materials that can change the ratio of continuous-fiber to thermoplastic resin or short-fiber-reinforced thermoplastic resin during printing. A nozzle for molding short-fiber or resin and a nozzle for molding continuous-fiber were arranged coaxially. The injection amount of the short-fiber or resin was dependent on the location. The results are summarized as follows:

(1) We developed a 3D printer with a continuous-fiber nozzle at the center of the screw that injects thermoplastic resin or short-fiber-reinforced thermoplastic resin. The amount of thermoplastic resin between the print paths can be varied, and the operability of the printer was validated.

(2) Owing to the inner continuous-fiber pipe of the coaxial double nozzle, protruding from the outer nozzle by *0.2* mm, it was possible to mold the fibers in a print path in which they are encased in thermoplastic resin.

(3) The molded tensile test specimens practically exhibited the same strength as the theoretical strength in the 0° tensile test, and the effects of fiber breakage that occurred during printing were observed to be minimal.

(4) The molded continuous-fiber-reinforced thermoplastic resin had a void ratio of *6.8* %; thus, the molding conditions require optimization.

Acknowledgments

Some of the experiments reported in this paper were supported by AGC Ltd. We would like to express our gratitude to all of those involved.

Appendix

As mentioned in Section 2.5, three adjustments to the pipe position were experimentally investigated. They include Types A–C, in which the pipe tip was placed 1 mm in the nozzle tip, protruded *0.2* mm from the nozzle tip, and protruded *0.5* mm from the nozzle tip, respectively. Fig. A1 shows the schematic representation of the pipe positions.

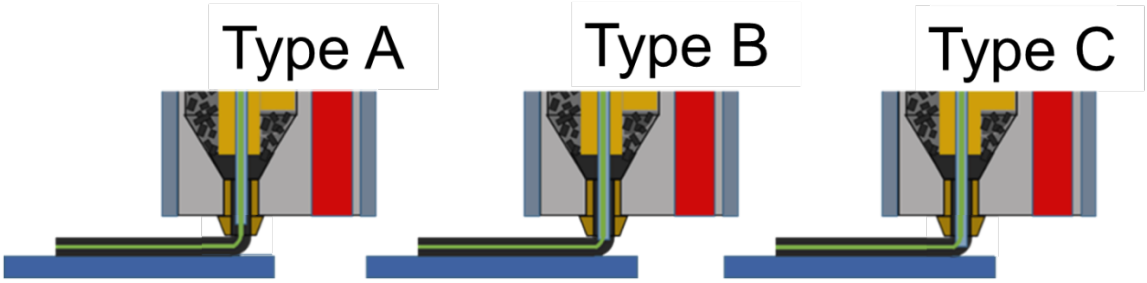

Fig. A1 Schematic representation of pipe position used for the nozzle for continuous-fiber filaments.

The solidified resin was fused to the bed or lower layer during lamination; thus, continuous fibers were fixed to the bed at that point. When the nozzle moved to the right (Fig. A1), the continuous fibers in the pipe were pulled by the nozzle because they were fixed on the left side, where the resin had solidified. Furthermore, the thermoplastic resin in the nozzle and near the outlet was molten. Thus, in the Type A state, the continuous fibers contacted the edge of the nozzle, and the fiber bundle ended at the top of the print path; therefore, the fiber bundle was not wrapped in the resin layer (short-fiber CFRP, abbreviated herein as sCFRP). This result was practically the same even when the heights of the pipe and nozzle were the same. Based on the above, Types B and C, were considered, and Type A was used for comparison. Fig. A2 shows the cross-sectional images of the printing path.

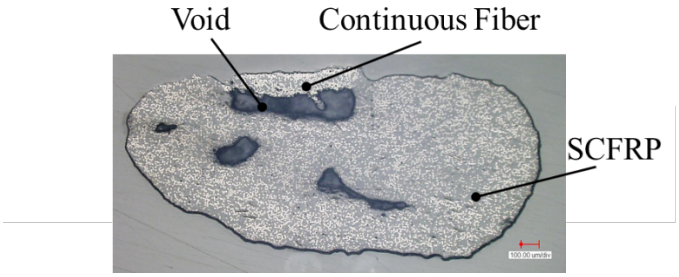

(a) Type A.

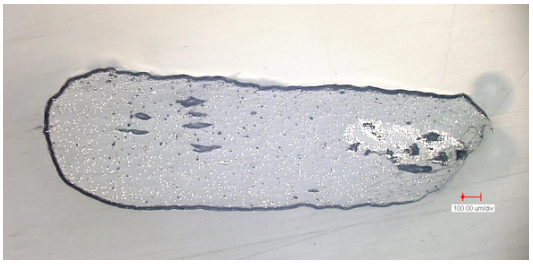

(b) Type B.

(c) Type C.

Fig. A2 Cross-sectional observations of the print path of Types A–C.

As shown in Fig. A2(a), in Type A, the continuous-fiber was fixed at the top end of the print path, and the sCFRP could not encase the continuous-fiber. In addition, the continuous-fiber filament was lifted from the printed thermoplastic resin, and a large void was formed on the underside of the continuous-fiber filament. In Type B (Fig. A2(b)), the continuous-fiber bundle successfully encased the sCFRP. Although voids still existed, they were relatively small. In Type C, the grooves created by the pipe remained. These grooves could become large voids during lamination.

We considered this phenomenon using a simple model. Fig. A3 shows the coordinate system for Type C, in which a groove is created in the print path by extending a pipe from the nozzle. The nozzle moved in the positive x-axis direction. A printing path with a groove created by the pipe was printed to the left of the nozzle.

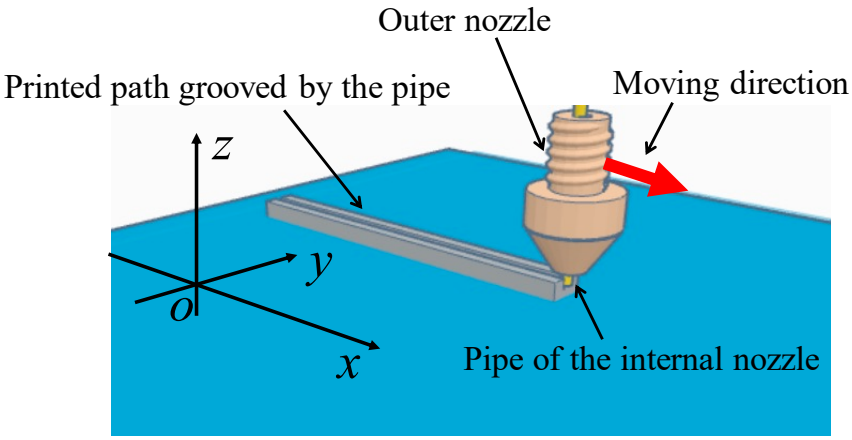

Fig. A3 Schematic representation of the printing process when the pipe makes a groove on the printed path.

Fig. A4 shows a schematic diagram of the nozzle movement, viewed from above. The double circles represent the coaxial double nozzle. When viewed from above the bed (above the z-axis in Fig. A3), the nozzle moved to the right in a straight line from A1 to A2 (Fig. A4). The inner diameter of the outer nozzle of the double nozzle is d_0, and the outer diameter of the inner pipe nozzle is d_i. The solid double circles in Fig. A4 represent the position of the double nozzle at time t_0 (central position, a_0).

t_1 ($t_1 > t_0$), when the nozzle moved a distance $L = (d_o + d_i)/2$ to the left, is indicated by a dashed double circle in Fig. A4 (central position, a_3). For simplicity, we only considered the A_1–A_2 line. The molten resin was injected into the right end of the inner pipe of the double nozzle (a_1, Fig. A4) at time t_0 (a_0). As the inner pipe nozzle moved to the right, a groove was created with a depth equal to the amount of pipe protrusion (d_h) from the tip of the outer nozzle. The width of the groove was the pipe diameter (d_i). Fig. A5 shows the schematic representation of a grooved printed path.

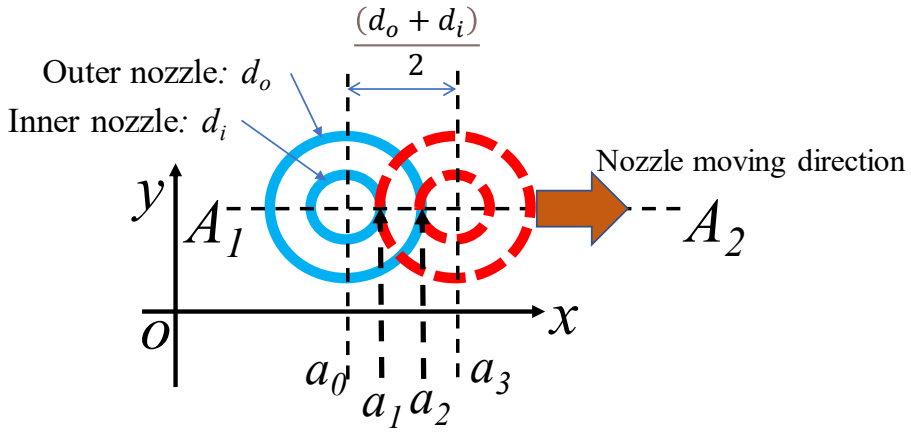

Fig. A4 Modeling of nozzle movement.

As shown in Fig. A5, the sCFRP (or thermoplastic resin) injected from the outer nozzle indicated by the broken line in Fig. A4 between a_1 and a_2 was scraped off to a depth of d_h by the pipe. The pipe protruded by the d_h from the tip of the outer nozzle.

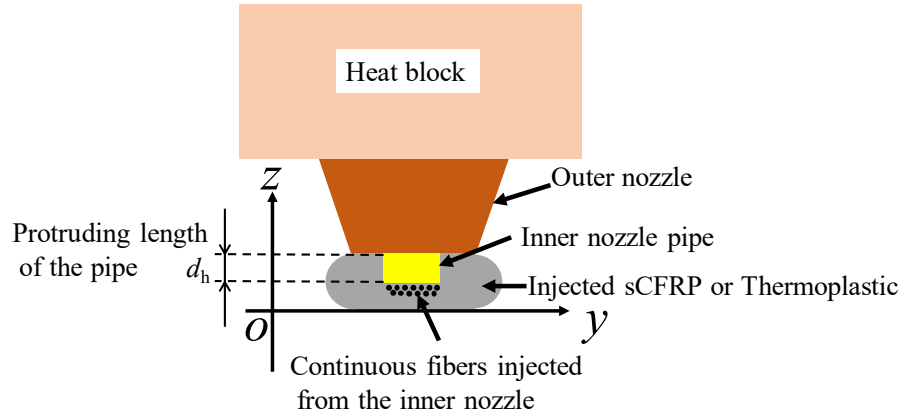

Fig. A5 Schematic representation of a grooved printed path.

The continuous fibers ejected from the pipe of the inner nozzle fused with the surrounding sCFRP at a position lower than the d_h (Fig. A5). Thus, the depth of the groove created by the pipe was equal to the d_h regardless of the continuous fibers. If the resin flow was not considered, this groove was backfilled by the ejection of sCFRP from the outer nozzle as the nozzle moved to the right (ejection of sCFRP between a_1 and a_2 on the A1–A2 line in Fig. A4). In an analysis of the 3D printing of sCFRP by Imaeda et al. using a particle method [17], the ejected sCFRP in the part that did not come into contact with the nozzle edge was solidified immediately. The groove created by the pipe did not remelt unless molten sCFRP was supplied from the outer nozzle when the pipe moved, and the movement of the resin due to melting was considered minimal.

For simplicity, the unit area injected from the outer nozzle and the injection volume per unit time was uniform and designated as W [mm/s], and the nozzle movement speed was V [mm/s] (generally, $W = V$). As shown in Fig. A4, on the A1–A2 line, a groove was created by the pipe movement when the right end of the pipe reached position a_1, and the outer nozzle at position a_1 completed the backfilling of the groove when the left end of the pipe reached position a_2. Considering that the nozzle movement distance was $L = (d_0 + d_i)/2$, the time Δt for the nozzle center position to move from a_0 to a_3 was given by $\Delta t = L/V$. However, the time until the left end of the pipe passed position a_1 was used for the pipe to create the

groove; thus, this movement time was not used to backfill the groove (Fig. A6). As the pipe passed from position a_1 to the position indicated by the dashed line in Fig. A6, it was not used to backfill the groove. At this time, the center of the nozzle was shifted to the right of a_0 by twice the radius of the pipe (i.e., the pipe diameter). Thus, it is necessary to subtract the time it takes for the nozzle to move the pipe diameter from the nozzle travel distance L, and the actual backfilling time was $\Delta t_T = (L - d_i)/V = (d_o - d_i)/(2V)$.

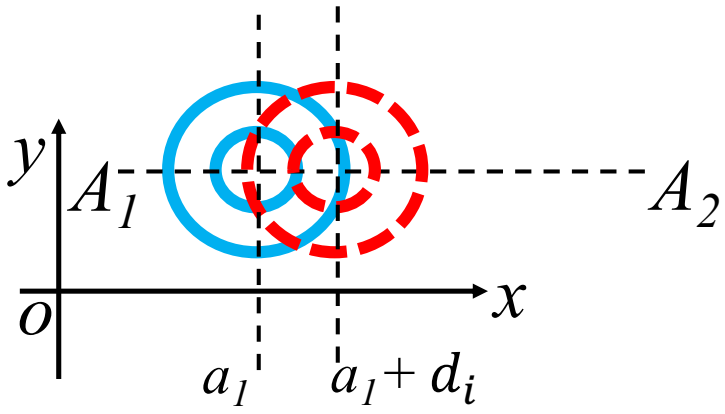

Fig. A6 Starting point of backfilling.

The volume of sCFRP injected per unit area in time Δt_T was $\Delta t_T W$. Thus, the height of the sCFRP injected per unit area into the groove made by the pipe was $\Delta t_T W$. If this exceeds the depth of the groove created by the pipe, the groove will be filled. As shown in Fig. A6, the depth of the groove created by the pipe was d_h. Thus, the following equation was obtained as the pipe installation condition:

$$\Delta t_T W > d_h. \tag{A1}$$

In the experiment, the injection speed $W = V = 100$ mm/min (1.67 mm/s); thus, Equation (A1) became

$$(d_o - d_i)/2 > d_h. \tag{A2}$$

The inner diameter of the outer nozzle was *2.5* mm, and the outer diameter of the pipe was *1.2* mm. By substituting these into Equation (A2), the following condition was obtained:

$$0.65 \text{ mm} > d_h. \tag{A3}$$

In Type B (Fig. A1), $d_h = 0.2$ mm, which fully satisfies Equation (A3). In Type C, $d_h = 0.5$ mm, which satisfies Equation (A3); however, the groove was not filled.

This was believed to be because when the d_h is deep, the pipe undergoes bending elastic deformation due to the resistance of the sCFRP being pushed aside (Fig. A7). The resistance pushing against the sCFRP caused the pipe to bend to the left, opposite the direction of the nozzle movement (to the right). This bending deformation was denoted as δ_b. The backfilling start time was delayed by the amount of δ_b. However, because the nozzle movement speed did not change, the backfilling end time did not change; thus, the time available for backfilling was reduced.

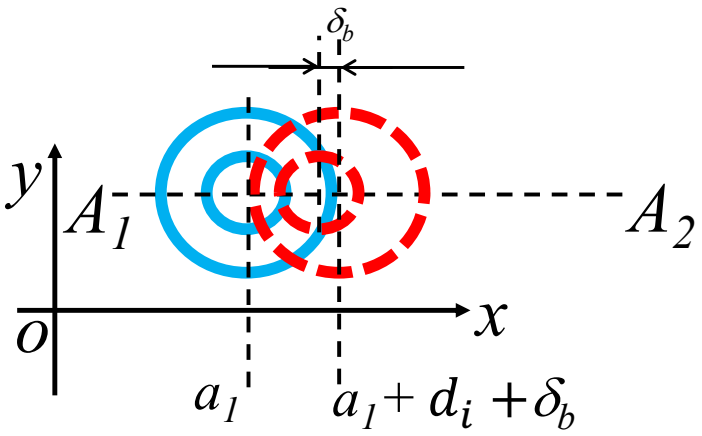

Fig. A7 Retardation of starting point of backfilling because of bending of pipe.

The cross-section in Fig. A2 shows continuous fibers just below the pipe groove, and it is clear that they had not been backfilled at all. This was presumably because the pipe was in contact with the left end of the nozzle (Fig. A7). As shown in Fig. 9, the pipe was fixed to the top of the motor mount; thus, the pipe length was approximately 220 mm. When a stainless steel pipe (outer and inner diameters of *1.2* and *0.8* mm, respectively) was used, the second moment of area was *0.081681* mm^4, and the load that causes a displacement of *0.6* mm at the tip of a cantilever beam with a length of *220* mm was only approximately *0.27* g. In addition, this was confirmed by the cross-sectional observation image shown in Fig. A2. It was expected that the pipe would move left and right because of the use of the screw. Thus, fundamental improvements are required to prevent the pipe from moving left and right; this will be addressed in the future.

We estimated the viscous resistance (F) when a pipe moves through molten sCFRP. Considering that the flow was very slow, and the resin was in contact with the pipe, which had reached its melting point, the surrounding resin was considered to be a molten viscous fluid. If we consider the pipe as a cylinder and use the Stokes approximation for a slow-moving viscous fluid around the cylinder [18], the F acting on the cylinder is given by the following equation:

$$F = 8\pi\mu U / \{1+2\log(L_a/a)\}. \tag{A4}$$

Here, μ is the viscosity coefficient, U is the fluid velocity, L_a is an arbitrary length, and a *is* the radius of the cylinder. Although the Stokes approximation around a cylinder is not accurate [18], it is simple. As an approximation, let $L_a = a$. Multiplied by the pipe extension length (depth of groove made by pipe) d_h as the length that receives the load, the following equation was obtained:

$$F = 2.67\pi\mu U d_h. \tag{A5}$$

The viscosity coefficient of PA-6 was approximately *2000* Poise near its melting point [19]. However, because PA-6 contains *10*% fiber by volume and was thought to rapidly solidify when it leaves the pipe [17], it was estimated to have an average value of *3000* Poise. The flow velocity, U, considering the speed of movement through the pipe, was calculated to be *0.2* g, which was close to *0.27* g. In reality, it was estimated that the reaction force F_f, caused by the continuous fibers being sheared at the end of the pipe, acted in the direction in which the pipe bent.

The deformation of the pipe due to viscous resistance acted in a direction that reduced the left side of Equation (A2); therefore, if we define this deformation as δ_1, the equation was modified as follows:

$$(d_o - d_i)/2 - \delta_l > d_h. \quad \text{(A6)}$$

However, for the bending of a cantilever beam, if F is the load at the tip, L_b is the length, and EI is the bending rigidity, the following equation was obtained:

$$\delta = FL_b^3/(3EI). \quad \text{(A7)}$$

Substituting Equation (A5) into F in Equation (A7) and then into Equation (A6), the following equation was obtained:

$$(d_o - d_i)/2\text{-}2.76\pi\mu UL_b^3 d_h/(3EI) > d_h. \quad \text{(A8)}$$

We used a viscosity coefficient of *3000* Poise in Equation (A8) and calculated, as mentioned earlier, that the condition was satisfied even when $d_h = 0.5$ mm. As previously mentioned, the F_f caused by the continuous-fiber being sheared at the end of the pipe bent the pipe. By inserting Equations (A7) into (A8), the following equation was obtained:

$$(d_o - d_i)/2 - 2.76\pi\mu UL_b^3 d_h/(3EI) - F_f L_b^3/(3EI) > d_h. \quad \text{(A9)}$$

In the viscosity coefficient model used in a study [16], when the rate dependency was ignored, the viscosity coefficient was approximately *1960* Poise near the melting point of PA-6. The viscosity coefficient may reach approximately *3000* Poise because of the presence of short fibers and solidification.

The exact effects of viscosity and continuous-fiber shearing are unknown; thus, it is convenient to divide the left side of Equation (A9) by a safety factor, *S.* Transforming Equation (A9) yielded the following:

$$(d_o - d_i)/2 > \{2.76\pi\mu UL_b^3/(3EI) + 1\}\, d_h + F_f L_b^3/(3EI) \quad \text{(A10)}$$

Here, if F_f can be measured, Equation (A10) can be calculated. If the external force that causes a *0.6*-mm displacement in the pipe is *0.27* g and the difference between the viscous force of *3000* Poise is *0.07* g, then Equation (A10) is no longer satisfied at $d_h = 0.5$ mm. The measurement of F_f will be investigated in the future.

Appendix data

Hole screw STL data <screw.stl here>

Printing process video https://youtube.com/shorts/4NwIi-WuFd0

References

(1) Schmitz B, 28th Jan, (2014), https://www.3dcadworld.com/worlds-first-carbon-fiber-3d-printer-makes-debut-solidworks-world/ (Access 2024/5/14).

(2) Namiki M, Ueda M, Todoroki A, Hirano Y, Matsuzaki R. 3D printing of continuous fiber reinforced plastic. SAMPE Tech Seattle 2014 Conference;2014:108061.

(3) Matsuzaki R, Ueda M, Namiki T, Jeong T, Asahara H, Horiguchi K, Nakamura T, Todoroki A, Hirano Y. Three-dimensional printing of continuous-fiber composites by in-nozzle impregnation. Scientific Reports. 2016;6:23058.

(4) Tian X, Liu T, Yang C, Wang Q, Li D. Interface and performance of 3D printed continuous carbon fiber reinforced PLA composites. Composites Part A: Applied Science and Manufacturing. 2016;88:198-205.

(5) Van Der Klift F, Koga Y, Todoroki A, Ueda M, Hirano Y, Matsuzaki R. 3D printing of continuous carbon fiber reinforced thermos-plastic (CFRTP) tensile test specimen. Open Journal of Composite Materials. 2016;6(1):18-27.

(6) Carbon Fiber 3D Printer: Markforged Mark Two Review: https://all3dp.com/carbon-fiber-3d-printer-markforged-mark-two-review (Access 2022/9/25).

(7) Todoroki A, Oasada T, Mizutani Y, Suzuki Y, Ueda M, Matsuzaki R, Hirano Y, Tensile property evaluations of 3D printed continuous carbon fiber reinforced thermoplastic composites. Advanced Composite Materials. 2020;29:147-162.

(8) Yamanaka Y, Todoroki A, Ueda M, Hirano Y, Matsuzaki R. Fiber line optimization in single ply for 3D printed composites. Open Journal of Composite Materials. 2016;6(4):121-131.

(9) Mikulionok I O, Radchenko L B. Screw extrusion of thermoplastic: General model of the screw extrusion. Russian Journal of Applied Chemistry. 2012;85:489-504.

(10) Whyman S, Arif K M, Potgieter J. Design and development of an extrusion system for 3D printing biopolymer pellets. The International Journal of Advanced Manufacturing Technology. 2018;96:3414-3428.

(11) Araki K, Nakamura K. Melt flow property of fiber reinforced Nylon and Polycarbonate. Journal of the Textile Machinery Society of Japan. 1988;41:T39-T47.

(12) Japan Gear Manufacturers Association, JGMA405-01:1978

(13) https://metoree.com/categories/2307/ (Access 2024/5/14).

(14) FILASTRUDER, https://www.filastruder.com/collections/filastruders-accessories/products/filastruder-kit?variant=323882043 (Access 2024/5/14)

(15) Koga Y, Todoroki A, Mizutani Y, Suzuki Y． Deflection of deposited short fiber and anisotropic mechanical properties of 3D printed isotropic short fiber reinforced plastics based on Fused Deposition Molding. Reinforced plastics. 2017;63(12):604-608. (in Japanese)

(16) Shirasu K, Yamaguchi Y, Hoshikawa Y, Kikugawa G, Tohmyoh H, Okabe T. Micromechanics study of short carbon fiber-reinforced thermoplastics fabricated via 3D printing using design of experiments. Materials Science and Engineering. A. 2024;891:145971.

(17) Imaeda Y, Todoroki A, Matsuzaki R, Ueda M, Hirano Y. Modified moving particle semi-implicit method for 3D print process simulations of short carbon fiber/polyamide-6 composites. Composites Part C: Open Access. 2021;6:100195.

(18) Imai I, “Fluid dynamics Part 1 20th Edition”, Physics selection 14, Shokabo Co., Ltd. 1993:333 (in Japanese) .